Chemical characterisation of benzene oxidation products under high and low NO_x conditions using chemical ionisation mass spectrometry

Michael Priestley[1*], Thomas J. Bannan[1], Michael Le Breton[1†], Stephen D. Worrall[1=], Sungah Kang[2], Iida Pullinen[2+], Sebastian Schmitt[2], Ralf Tillmann[2], Einhard Kleist[7], Defeng Zhao[2-], Jürgen Wildt[2,7], Olga Garmash[4], Archit Mehra[1^], Asan Bacak[1~], Dudley E. Shallcross[3,5], Åsa M. Hallquist[8], Mikael Ehn[4], Mattias Hallquist[6], Astrid Kiendler-Scharr[2], Thomas F. Mentel[2], Gordon McFiggans[1], Hugh Coe[1], Carl J. Percival[1‖]

[1]Centre for Atmospheric Science, Department of Earth and Environmental Sciences, University of Manchester, Manchester, M13 9PL, UK

[2]Institut für Energie und Klimaforschung, IEK-8, Forschungszentrum Jülich, Jülich, Germany

[3]School of Chemistry, The University of Bristol, Cantock's Close BS8 1TS, UK

[4]Institute for Atmospheric and Earth System Research/Physics, Faculty of Science, University of Helsinki, 00014 Helsinki, Finland

[5]Department of Chemistry, University of the Western Cape, Bellville, South Africa

[6]Department of Chemistry and Molecular Biology, University of Gothenburg, 412 96, Gothenburg, Sweden (* Now at)

[7]Institut für Bio- und Geowissenschaften, IBG-2,,Forschungszentrum Jülich GmbH, Jülich, Germany

[8]IVL Swedish Environmental Research Institute, Gothenburg, Sweden

[‖] Now at Jet Propulsion Laboratory, 4800 Oak Grove Drive, Pasadena, CA 91109

[+] Now at Department of Applied Physics, University of Eastern Finland, 702132 Kuopio, Finland

[=] Now at Aston Institute of Materials Research, School of Engineering and Applied Science, Aston University, Birmingham, B4 7ET, UK

[†] Now at Volvo Group Trucks Technology, L3 Lundby, Gothenburg, Sweden

[~] Now at Turkish Accelerator & Radiation Laboratory, Ankara University, Institute of Accelerator, Technologies Gölbaşı Campus, 06830 Golbasi / Ankara, Turkey

[^] Now at Faculty of Science and Engineering, University of Chester, CH2 4NU, UK

[-] Now at Department of Atmospheric and Oceanic Sciences & Institute of Atmospheric Sciences, Fudan University, Shanghai, China

Corresponding author: Michael Priestley (michael.priestley@gu.se)

Abstract

Aromatic hydrocarbons are a class of volatile organic compounds associated with anthropogenic activity and make up a significant fraction of urban VOC emissions that contribute to the formation of secondary organic aerosol (SOA). Benzene is one of the most abundant species emitted from vehicles, biomass burning and industry. An iodide time of flight chemical ionisation mass spectrometer (ToF-CIMS) and nitrate ToF-CIMS were deployed at the Jülich plant atmosphere chamber as part of a series of experiments examining benzene oxidation by OH under high and low NO_x conditions, where a range of organic oxidation products were detected. The nitrate scheme detects many oxidation products with high masses ranging from intermediate volatile organic compounds (IVOC) to extremely low volatile organic compounds (ELVOC), including C_{12} dimers. In comparison, very few species with $C_{\geq 6}$ and $O_{\geq 8}$ were detected with the iodide scheme, which detected many more IVOC and semi volatile organic compounds (SVOC) but very few ELVOC and low volatile organic compounds (LVOC). 132 and 195 CHO and CHON oxidation products are detected by the iodide ToF-CIMS in the low and high NO_x experiments respectively. Ring breaking products make up the dominant fraction of detected signal and 21 and 26 of the products listed in the master chemical mechanism (MCM) were detected. The time series of highly oxidised ($O_{\geq 6}$) and ring retaining oxidation products (C_6 and double bond equivalent = 4) equilibrate quickly, characterised by a square form profile, compared to MCM and ring breaking products which increase throughout oxidation exhibiting saw tooth profiles. Under low NO_x conditions, all CHO formulae attributed to radical termination reactions of 1st generation benzene products and 1st generation autoxidation products are observed. Several N containing species that are either 1st generation benzene products or 1st generation autoxidation products are also observed under high NO_x conditions. Hierarchical cluster analysis finds four clusters, of which two describe photo-oxidation. Cluster 2 shows a negative dependency on the NO_2/NO_x ratio indicating it is sensitive to NO concentration and thus likely to contain NO addition products and alkoxy derived termination products. This cluster has the highest average carbon oxidation state ($\overline{OS_C}$) and the lowest average carbon number. Where nitrogen is present in a cluster member of cluster 2, the oxygen number is even, as expected for alkoxy derived products. In contrast, cluster 1 shows no dependency on the NO_2/NO_x ratio and so is likely to contain more NO_2 addition and peroxy derived termination products. This cluster contains less fragmented species, as the average carbon number is higher and $\overline{OS_C}$ lower than cluster 2, and more species with an odd number of oxygen atoms. This suggests that clustering of time series which have features pertaining to distinct chemical regimes e.g. NO_2/NO_x perturbations, coupled with *a priori* knowledge, can provide insight into identification of potential functionality.

1. Introduction

Benzene is an aromatic volatile organic compound (VOC) commonly used as a vehicular fuel additive (Verma and Des Tombe, 2002) and as a chemical intermediate in the manufacture of a range of products e.g. detergents (Oyoroko and Ogamba, 2017), lubricants (Rodriguez *et al.*, 2018), dyes (Guo *et al.*, 2018) and pesticides (Wang *et al.*, 2014). Whilst current global estimates of benzenoid (molecules containing a benzene ring) emission to the atmosphere by vegetation is of a comparable order to that of anthropogenic activity (~ 5 times lower, Misztal et al. 2015), and background concentrations of benzene are enhanced by increased biomass burning (Archibald *et al.*, 2015), emission of benzene to the urban atmosphere is dominated by vehicle exhausts (Gentner *et al.*, 2012) and solvent evaporation (Hoyt and Raun, 2015). As well as a toxin (Snyder, Kocsis and Drew, 1975) and carcinogen (Ruchirawat *et al.*, 2005, 2007; Bird *et al.*, 2010), benzene is photochemically active and contributes to the formation of ozone (O_3) and secondary organic aerosol (SOA), both of which act to modify the climate and contribute to poor air quality (Henze *et al.*, 2007; Ng *et al.*, 2007). SOA formation from benzene has previously been quantified with a focus on the contribution from smaller mass, ring breaking reaction products such as epoxides (Glowacki, Wang and Pilling, 2009) and dicarbonyl aldehydes (e.g. O'Brien *et al.*, 1983; Johnson *et al.*, 2005). For example the 37% of the glyoxal formed in the LA basin is estimated to derive from aromatic sources

(Knote *et al.*, 2014). These smaller ring breaking products typically make up a larger fraction of SOA mass than the ring retaining products (Borrás and Tortajada-Genaro, 2012) and so have traditionally been the main focus for SOA quantification. Other major, toxic benzene oxidation products such as catechol, nitrophenol and maleic anhydride are also known components of SOA (Borrás and Tortajada-Genaro, 2012).

More recently the autoxidation mechanism has been demonstrated to occur in aromatic systems (Wang *et al.*, 2017, Wang *et al.*, 2020; Molteni *et al.*, 2018; Tsiligiannis *et al.*, 2019; Garmash *et al.*, 2020; Mehra *et al.*, 2020) producing highly oxygenated organic molecules (HOM, defined as containing 6 or more oxygen atoms which is a product of the autoxidation mechanism) incorporating up to 11 oxygen atoms (Bianchi *et al.*, 2019). The autoxidation mechanism of intra molecular H shifts from the carbon backbone to the peroxy radical centre forming peroxide groups is consistent with other VOC systems (Rissanen *et al.*, 2014) initiated by a variety of different oxidants (e.g. Mentel et al. 2015; Berndt et al. 2016). The inclusion of an alkyl group to a benzene ring facilitates HOM formation (Wang *et al.*, 2017) as a consequence of the greater degrees of freedom afforded to the molecule. Whilst benzene is not the most reactive of aromatic VOCs, $\tau_{OH} \approx 9.5$ days for benzene vs. $\tau_{OH} \approx 6$-10 hours for xylenes ($[OH] = 2.0 \times 10^6$ molecules cm^{-3}, Atkinson and Arey, (2007)), it is ubiquitous in the urban environment and is the simplest C_6 aromatic ring system to study.

Oxidation of benzene occurs nearly exclusively via hydroxyl radical (OH) addition to form the cyclohexadienyl radical/benzene-OH adduct, which subsequently adds O_2 to form the hydroxycyclohexadiene peroxy radical (C_6H_6-OH-O_2) (Volkamer *et al.*, 2002) (Fig. 1). Two subsequent reaction pathways are postulated for this peroxy radical: either elimination of HO_2 yields phenol and secondary OH attack must occur again; or an endocyclic di-oxygen bridged carbon centred radical intermediate is formed by the addition of the peroxy group to (typically a β-carbon (Glowacki, Wang and Pilling, 2009)). This di-oxygen bridge carbon centred radical may add another O_2 and form a peroxy radical (named as BZBIPERO2 in the master chemical mechanism, MCM, Saunders et al. (2003)). However it is not known if autoxidation may continue to form a second oxygen bridged radical, described as type II autoxidation (Molteni *et al.*, 2018, Fig 1, BZBIPERO2-diB), or form a hydroperoxide carbon centred radical, formed through intra molecular hydrogen abstraction (type I autoxidation). At each step, termination of the peroxy radical to hydroxyl, hydroperoxyl, nitrate, peroxy nitrate or reduction to an alkoxy radical is possible, from which further termination via formation of a nitrite, nitro- or acyl group can occur.

Typically the presence of NO_x alters the product distribution of VOC oxidation and reduces SOA formation (e.g. Stirnweis et al. 2017). With other atmospherically relevant VOC precursors of SOA e.g. isoprene or monoterpenes, high NO conditions can supress SOA formation (Wildt *et al.*, 2014; Sarrafzadeh *et al.*, 2016) as reduction of RO_2 to RO ultimately leads to fragmentation of the RO species (Surratt *et al.*, 2006; Nguyen *et al.*, 2015), but it can also form epoxides, aldehydes and hydroperoxides which readily partition to the aerosol phase and contribute to SOA growth (Surratt *et al.*, 2010).

The further reaction of NO_x with oxygenated VOCs produces species including nitro organics, nitrates, peroxy nitrates and peroxyacyl nitrates (Atkinson, 2000) that can also condense and contribute to SOA formation. Under conditions where NO_x is present in moderate amounts, the HO_2:OH ratio is low as HO_2 is reduced by NO to form OH. This allows more OH oxidation to occur and less termination of RO_2 by HO_2 to occur; whereas under low NO_x conditions VOC consumption is lower, as OH recycling from HO_2 relies on the slower $HO_2 + O_3$ reaction (Atkinson, 2000). Here low and high NO_x are relative terms and are defined by the available VOC. This reduction of the HO_2:OH ratio as a function of NO has been observed at Mace Head, Ireland where clean low NO_x marine influenced air can be contrasted with polluted NO_x containing continental air (Creasey, Heard and Lee, 2002). In that instance, an increase in NO concentration from 0.01 ppb to 1 ppb reduces the HO_2:OH ratio from 200:1 to 10:1.

The autoxidation mechanism is known to form biogenic HOM, and as a consequence SOA, in ambient rural environments (e.g. Ehn et al. 2014). The mechanism is increasingly a competitive process in urban and suburban environments where NO_x concentrations have seen significant reductions in recent years (Praske *et al.*, 2018). These low concentrations of NO_x (0.1 - 1's ppb) have been shown to enhance local oxidant production and drive an increase in biogenic HOM formation (Pye *et al.*, 2019). Aromatic HOM formation by OH at relevant urban NO_x concentrations has been demonstrated (Tsiligiannis *et al.*, 2019; Zaytsev *et al.*, 2019; Garmash *et al.*, 2020; Mehra *et al.*, 2020).

ToF-CIMS is a measurement technique frequently used to probe VOC oxidation due to the ability to detect many low concentration compounds simultaneously in real time (e.g. Chhabra et al. 2015). As a result of the sensitivity of the nitrate ionisation scheme towards HOM, this reagent ion is typically used to study the autoxidation mechanism and HOM formation. However, to observe carbon in a diverse range of forms, e.g. different oxidation states and of different functionalities, multiple ionisation schemes are required as they are sensitivities towards different OVOCs (e.g. Isaacman-VanWertz *et al.*, 2017; Riva *et al.*, 2019). These methods, combined with other measurement techniques, have been demonstrated to enable the complete observation of all the reacted carbon within a system (carbon closure) (Isaacman-Vanwertz *et al.*, 2018).

In this study, the oxidation of benzene and its oxidation products by OH under high and low NO_x conditions are investigated in the Jülich plant atmosphere chamber (JPAC) (Mentel *et al.*, 2009, 2015) with two time of flight chemical ionisation mass spectrometers (ToF-CIMS) using the iodide and nitrate ionisation schemes. The ionisation schemes are compared to assess the similarities in detected oxidation products in terms of molecular identification and bulk properties. Mechanistic investigations to assess the ability of the iodide CIMS to detect species that currently aren't accounted for i.e. HOM and those described in the MCM are investigated. Additionally high and low NO_x conditions are probed. As sensitivities for the iodide CIMS are lacking, an exploration of product descriptions is made using bulk analysis, as well as broad groupings defined by bulk properties. Finally, the application of hierarchical clustering analysis (HCA) is used to provide the basis of a methodology to assess the time series behaviour of oxidation products that can further aid molecular identification e.g. by inferring potential functionality.

2. Methods and Experimental

The experiments were performed in a 1450 L borosilicate chamber of the Jülich Plant Atmospheric Chamber (JPAC) described elsewhere (Mentel *et al.*, 2009). The chamber is operated as a continuously stirred tank reactor with modifications as described in Mentel *et al.* (2015). A fan made of Teflon provides typical mixing time of less than 2 minutes. The total flow in and out the chamber was 30 L min^{-1} resulting in an average residence time in the chamber of ~2900 seconds or 48 minutes. Benzene (Merck, ≥ 99.7%) was introduced into the chamber by flowing purified ambient air over a diffusion source to maintain a constant concentration and was monitored by recording the inlet and outlet concentrations by quadrupole proton transfer mass spectrometry (PTR-MS). The

PTR-MS (IONICON) was calibrated using a benzene diffusion source (Garmash *et al.*, 2020). The difference between the outlet and inlet concentrations, measured at a 2 minute time resolution and switched every 25 minutes, describes the reacted benzene, from which the OH concentration is calculated. The loss of benzene by photolysis was found to be negligible as measured by Q-PTR during experiments where only benzene was introduced into the chamber, in accordance with observations in the literature (Kamps *et al.*, 1993; Fally, Carleer and Vandaele, 2009).

Experiment	Benzene In (SS) / ppb	Ozone In (SS) / ppb	RH at 288K / %	NO In (SS) / ppb	$J_{(O1D)}$ / 10^{-3} s^{-1}	J_{NO2} / 10^{-3} s^{-1}	OH_{SS} / 10^7 molecules cm^{-3}	Equivalent OH dose / days	Chamber residence time / seconds
0	290 (245)	115 (40)	60	0 (0*)	5.0	0.00	6	5	~2900
1	65 (55)	95 60)	60	38 (<1**)	2.60	4.30	6	5	~2900
1	65 (56)	95 (50)	60	38 (0)	2.60	0.00	6	5	~2900

Table 1. Summary of selected experiments performed at JPAC used in this study. Two photolysis states are reported for the NO_x containing studies. The first describes steady state concentrations with J_{NO2} (UVA) and ultra violet (TUV) light on, the second with only the J_{O1D} (TUV) light on. OH equivalent dose is based on 10^6 OH molecules cm^{-3}. * NO_2, background from VOC catalyser. ** not measured, estimated from experiment with similar NO_x addition, O_3 and OH.

OH is generated by photolysis of O_3 by a UV lamp ($\lambda < 254$ nm, Philips, TUV 40W herein termed TUV) and the subsequent $O(^1D)$ reaction with H_2O. O_3 is introduced to the chamber by a separate line to the benzene and was monitored by UV absorption (Model 49, Thermo Environmental instruments). OH concentrations are calculated when steady state conditions (ss) are reached according to the equation below and are described in detail elsewhere (Garmash *et al.*, 2020). The chamber volume (V =1450 L) divided by the flow rate (F = 30 slm) is residence time in the chamber (t=2900 s). The rate coefficient for the reaction of benzene with OH, $k_{Benzene+OH} = 1.2x10^{-12}$ cm^3 s^{-1}, was taken from (IUPAC, 2008). Verification experiments were done by introducing 1,8-cineole into the chamber, which confirmed the calculated OH concentrations to be within 6 - 12% (Garmash et al., 2020). Integrating the OH concentration over the residence time gives an equivalent OH dosage that may be compared to atmospheric levels. Here OH equivalent doses are equivalent to approximately 5 days of oxidation at a relevant atmospheric OH concentration (10^6 molecules cm^{-3}).

$$[OH]_{ss} = \frac{[Benzene]_{in} - [Benzene]_{out}}{[Benzene]_{in}} \frac{1}{k_{Benzene+OH}\,(\frac{V}{F})}$$

For the high NO_x experiment, NO (Linde, 120 ± 5 ppm NO in N_2) was injected into the chamber via a separate perfluoro alkoxy alkane (PFA) line. The NO input of 20 ppb was measured by chemiluminescence (CLD 770 and PLC 760, Eco Physics). Twelve discharge lamps termed UVA (HQI, 400 W/D; Osram, Munich, Germany) were activated to photolyse NO_2 ($J_{NO2} = 4.3x10^{-3}$ s^{-1}) to increase the NO/NO_2 ratio, although NO_2 remains the dominant NO_x compound. More than half of the NO_x is consumed by reaction of NO_2 with OH and organic nitrate formation. About 10% of the remaining NO_x exists as NO for the given O_3 and J_{NO2}. Considering reactions of NO with RO_2

this fraction is even less. At the end of the experiment, the TUV lamp was kept on and the UVA lamps switched off. Temperature and humidity were maintained at 288 ± 1 K and 67 ± 2 % through the experiments. The experimental conditions are summarised in Table 1. It is expected that as the NO_x concentration decreases, peroxy radical lifetime is much longer than the required time scale for autoxidation hydrogen shifts (Praske *et al.*, 2018) and so autoxidation products can be expected in this low NO_x case here ($\leq$ 300 pptv). Where the UVA lamps are active, the NO/NO_x ratio is increased, thus increasing the ratio of RO/RO_x ($RO + RO_2$). The high NO_x condition for the iodide ToF-CIMS comparison (section 3.3) is performed when $J_{NO2} = 0\ s^{-1}$.

2.1. ToF-CIMS instrumentation

Iodide

The University of Manchester ToF-CIMS has been described by Priestley et al. (2018). The iodide ToF-CIMS ion molecule reaction region (IMR) was held at a constant pressure of 100 mbar by a scroll pump (Agilent SH-112) controlled with a servo control valve placed between the scroll pump and the IMR. The short segmented quadrupole (SSQ) region was held at 1.30 mbar by a second scroll pump (Triscroll 600). Chamber air was drawn into the IMR via a critical orifice at 2.2 slm where it mixed with I^- ions. The reagent I^- ions were created by flowing 10 standard cubic centimetres per minute (sccm) of nitrogen (N_2) over a methyl iodide (CH_3I) permeation tube made of 1/8” PFA and held at 40°C. This flow met 2 slm N_2 and was flowed through a ^{210}Po 10 mCi alpha emitting reactive ion source (NRD Inc.). The mass calibration was performed for 7 known masses: NO_3^-, I^-, $I^-.H_2O$, $I^-.HCOOH$, $I^-.HNO_3$, I_2^- and I_3^-, covering a mass range of 62 to 381 *m/z*. The mass calibration was fitted to a 3rd order polynomial and was accurate to within 2 ppm, ensuring peak identification was accurate below 20 ppm. The resolution was 3231 at 127 *m/z* and 3720 at 381 *m/z*. The inlet to the I^- ToF-CIMS sampled from the middle of the chamber and was comprised of 50 cm 1/4” O.D. PFA tubing giving residency time of <1.5 s.

Formic acid calibrations and chamber and instrumental backgrounds were taken before every experiment to assess instrument sensitivity changes. Backgrounds were performed by overflowing the CIMS inlet with N_2 and calibrations were performed by flowing 50 sccm N_2 over a formic acid permeation tube held at 40°C. The formic acid sensitivity was 3.15 ± 0.26 Hz ppt^{-1} (2σ) measured as a 5 minute average normalised to 10^6 Hz iodide. The background was 2.72 ± 0.66 ppt (2σ) measured as a 5 minute average normalised to 10^6 Hz iodide. The limit of detection (3σ) was 100 ppt. Calibration of all detected masses was not possible, so data are presented either as signal (Hz) from the instrument or as a number of species.

It is not possible to identify a compound from its formula alone. Oxidation is initiated with OH addition to the benzene ring, but fragmentation occurs and so the OH moiety may be lost; additionally multiple OH attacks make the counting of oxygen more difficult (Garmash *et al.*, 2020). It is for these reasons that RNO_x species are described more generally and any discussion of compound classes is speculative. Data analysis was performed using the Tofware (V 3.1.0, (Stark *et al.*, 2015)).

Nitrate

The Jülich ToF-CIMS with nitrate ionisation is described elsewhere (Garmash *et al.*, 2020). Chamber air was drawn into an Eisele type inlet at 9 slm where it merges with a 20 slm sheath flow of nitrogen that contains nitrate ions (NO_3) for approximately 200 ms. These ions are generated by flowing 10 sccm dry nitrogen through a wash bottle containing nitric acid (HNO_3, Aldrich, 70%) that pass through a ^{241}Am alpha emitting source. The inlet flow enters the instrument through a 300 µm diameter aperture after which the ions are collimated and energetically homogenised through a series of differentially pumped chambers.

Mass calibration is performed on nitrate, its dimer and trimer ions, NO_3, $NO_3.HNO_3$ and $NO_3.(HNO_3)_2$ and hexafluoropentanoic acid (NO_3.HFPA adduct), providing an accurate mass range up to 326 *m/z*. The resolution was ~4000 at 125 *m/z*. The inlet to the instrument sampled from the middle of the chamber by a 1m 1/4” O.D stainless steel tube.

2.2. Calculation of average carbon oxidation state ($\overline{OS_c}$)

Average carbon oxidation state $\overline{OS_c}$ (Kroll *et al.*, 2011) is commonly used to describe the degree of oxidation within a complex oxidation reaction. It is calculated using the oxygen to carbon ratio (O:C), hydrogen to carbon ratio (H:C) and the nitrogen to carbon ratio (N:C) and assumes nitrogen is in the form of nitrate where the oxidation state of N (OS_N) is +5 :

$$\overline{OS_c} = (2 \times O{:}C) - H{:}C - (5 \times N{:}C)$$

It is more difficult to justify this assumption for gas phase data and as this work explores different N-containing functional groups, this nitrate assumption cannot be used. Instead of assuming all N is in the form of nitrate, a range of OS_N (5+, 3+ and 0) are considered and $\overline{OS_c}$ is calculated as a range from a theoretical minimum, where all N is considered nitrate (5+), to a theoretical maximum, where all N is considered cyanate (0). Nitro and nitroso compounds are also considered (3+), but amines and amides are not as they are not expected to be present in the system. As neither the maximum or minimum OS_N is a likely or an accurate description of the system, they merely represent theoretical limits to calculate $\overline{OS_c}$; the true value will lie somewhere in the middle, in all likelihood between the mean and lower limit as most species are expected not to be cyanates. The $\overline{OS_c}$ reported here is the mean average of three scenarios where all N is considered to exist in 0, 3+ or 5+ oxidation states. This methodology reduces the accuracy of the reported $\overline{OS_c}$ but it clearly and accurately presents the $\overline{OS_c}$ range.

In this document $\overline{OS_c}$ are reported as a function of carbon number. The variation in $\overline{OS_c}$ between all CHON of the same carbon number is much greater than the variability in $\overline{OS_c}$ of a single CHON compound as a consequence of varying OS_N for that compound.

Where a species has the form $RNO_{1,2}$ the species is considered to be either a cyanate or hydroxy cyanate and the OS_N is set to 0. For RNO_3 species the nitrogen is considered to be either a dihydroxy cyanate or a hydroxy RONO or RNO_2 compound and so OS_N is set to either 0 or 3+. $RNO_{>3}$ have OS_N set to 0, 3+ or 5+. This leads to the modification of the $\overline{OS_c}$ parameterisation:

$$\overline{OS_c} = (2 \times O{:}C) - H{:}C - (OS_N \times N{:}C)$$

$$OS_N = 0 \; if \; nO = \leq 2$$

$$OS_N = [0, 3] \; if \; nO = 3$$

$$OS_N = [0, 3, 5] \; if \; nO > 3$$

2.3. Hierarchical Cluster Analysis (HCA)

Hierarchical cluster analysis (HCA) is an analytical technique used to simplify datasets containing large numbers of individual observations into groups or clusters defined by their similarity with the aim of increasing interpretability of the dataset. HCA is an agglomerative technique which allows for the successive merging of individuals or clusters to form larger clusters. Due to the complex nature of atmospheric oxidation and the detection of many oxidation products by mass spectrometry, it is common practice to reduce the dimensionality of mass spectrometry datasets in order to better describe bulk properties of the process being studied (Sekimoto *et al.*, 2018; Buchholz *et al.*, 2019; Isokääntä *et al.*, 2020; Koss *et al.*, 2020) with HCA being one such method. HCA is independent of calibration as it relies on relative differences between time series’ rather than exact concentrations, making it a suitable technique to apply to mass spectrometry data where authentic standards do not exist and individual calibrations are next to impossible. The final number of clusters is selected based on the distance between them and is determined by the user. Here we use HCA to group the time series’ of benzene oxidation products to investigate its utility as a tool for investigating oxidation processes or product properties where the reaction occurs in a continually stirred flow reactor.

In order to use HCA the linkage criterion and distance metric must be selected. The root of the sum of the squares of a pair of observations (time series), A and B, (i.e. the Euclidean distance) is chosen as the distance metric to define the similarity of the time series’ at each time step, t.

$$d_{A,B} = \sqrt{\sum_{t} (A_t - B_t)^2}$$

The Ward linkage criterion was chosen to determine the distance between sets of observations (U, V, which can be single or multimember clusters) as it gave similar or more interpretable results compared with other linkage criteria. Here, the sum of the squares of the cluster members (x_i where i iterates over the members U, V or their agglomeration) from their cluster means (m_U, m_V or $m_{U \cup V}$) are calculated. This is performed for the two candidate clusters for agglomerating (U, V) and for the new cluster they would form through agglomeration (U∪V). The difference in the sum of the squares between this potential merged cluster and the initial two candidate clusters is the distance used to assess whether the agglomeration of the candidate clusters is acceptable:

$$d_{U,V} = \sum_{i \in U \cup V} \|x_i - m_{U \cup V}\|^2 - \left(\sum_{i \in U} \|x_i - m_U\|^2 - \sum_{i \in V} \|x_i - m_V\|^2 \right)$$

When the increase in the sum of the squares (i.e. distances) is minimal after agglomerating the two candidate clusters, the new cluster is formed. Here, the time series for all CHO and CHON compounds from the iodide ToF-CIMS measurements were selected for clustering. Time series were scaled between 0-1 to remove the effect of their differing magnitudes and focus on the changes in trends. The scaled time series were then smoothed to a 10 minute average to remove noise that may affect the results of the HCA. This treatment is similar to other studies using HCA with mass spectrometric data (e.g. Koss *et al.*, 2019). The analysis was implemented using the cluster.hierarchy module from SciPy (1.2.0) scientific python library using Python 3.6.

3. Results and Discussion

We detect a range of benzene oxidation products, including many with the same formula as those listed in the MCM, as well as highly oxidised species with both ToF-CIMS instruments. Well resolved peaks at a given unit mass were frequently observed in the I^- spectrum. The separation between the I^- ion cluster with its large negative mass defect and the positive defect (excess) of the high H containing deprotonated species allows good peak separation at the resolution of the ToF-CIMS (Fig 2). Beyond I^- and H_2O, the largest adduct signals we identified with the I^- CIMS were low mass species: formic acid (CH_2O_2), nitric acid (HNO_3), CH_2O_3, $C_3H_6O_3$, HONO, $C_4H_4O_3$ and $C_3H_8O_3$. The prevalence of these ions is likely due to instrument sensitivity rather than chemistry.

3.1. Organic product distributions: comparison of nitrate and iodide ionisation

Forty-two formulae are found to be common in the low NO_x experiment between the two instruments representing the overlap of oxidation product signals of which 20 are C_6 compounds and the rest have lower carbon numbers. The time series behaviour of the signals at the start of oxidation is highly variable and is specific to each instrument and ion measured by that instrument as oxidant levels and wall partitioning equilibrates. Typically, the level of highly oxidised species increases significantly from the outset but relaxes to lower levels rapidly before they grow again to reach steady state. This early transient maximum spiking behaviour has been observed in other studies investigating VOC oxidation using the nitrate ToF-CIMS (e.g. Ehn et al. 2014) and is thought to be a consequence of a mixture of two phenomena that could include a latent aerosol sink shifting the equilibrium species from the gas to the aerosol phase as well as the dynamic nature of oxidant concentrations (mainly adaptation of O_3) before the steady state is reached and mixing is totally homogenous. The iodide CIMS measures a delayed response from wall equilibration processes (Krechmer *et al.*, 2016; Pagonis *et al.*, 2017) making the detection of these rapid changes more challenging. For the range of species measured here, the variability between the two measurements for the same species vary (Fig S1). In general the nitrate observes square waveforms whereas the iodide observes saw tooth waveforms. Where the agreement is particularly bad it is most likely that different isomers contribute to the different signals measured on the two instruments.

The nitrate ionisation scheme detects a greater number of higher mass species with a higher oxygen content (Fig 3c, 3e) and higher $\overline{OS_c}$ (Fig 3h, 0.84 vs 0.42), whereas the iodide ionisation scheme detects lower mass compounds with a lower oxygen number and lower $\overline{OS_c}$, as has been reported elsewhere in different VOC oxidation systems (e.g. Isaacman-VanWertz *et al.*, 2017). The average mass of a nitrate adduct (not including the reagent ion) is ~240 g mol^{-1} with ~30% of that attributable to oxygen, whereas the average mass of an iodide adduct is 140 g mol^{-1} with ~20% attributable to oxygen (Fig 3g).

The nitrate CIMS is able to detect a greater number of high mass species greater than C_6 including a large number of dimers (C_{12}) whereas the iodide scheme did not detect many species greater than C_6 in this instance but did measure a greater number of low C molecules compared to the nitrate (Fig 3a). Few species greater than C_{12} are detected with either reagent ion, suggesting that in this system their formation was not likely, as both the nitrate and iodide ionisation schemes are capable of detecting >C_{20} compounds (e.g. Mohr *et al.*, 2019). The iodide scheme detects a maximum number of molecules containing O_3 and O_4 and very few with more than O_7 (Fig 3c). The nitrate scheme observes a broad range of oxygen numbers peaking between O_9 and O_{11} but up to O_{18}. Iodide detects an average H:C/O:C of ~1.5 whereas nitrate detects H:C/O:C of approximately 1.1 due to higher O:C ratios (Fig 3f). Detection of molecules with greater than C_6 that are not C_{12} dimers are likely formed through peroxy radical cross reactions.

With both nitrate and iodide ionisation, the maximum variation in oxygen number per molecule is detected for C_6 compounds (Fig 4a) although for nitrate this is closely followed by C_{12} i.e. C_6 dimers as well as C_5, C_9 and C_{10} compounds. The nitrate CIMS detects approximately half the number of low oxygen content (O_{2-4}) (and N containing) oxidation products compared to the iodide CIMS. Subsequently, $\overline{\mathrm{OS}_C}$ as a function of carbon number differs between the ionisation schemes at higher carbon numbers (Fig 4b). Below C_8 the $\overline{\mathrm{OS}_C}$ broadly agree however above C_8 the iodide observes negative $\overline{\mathrm{OS}_C}$ whereas nitrate observes positive values. This is likely due to the detection of different isomers, which become more prevalent at these at these higher masses.

The saturation concentrations (C*) of the detected species were calculated using the relation of Mohr *et al.* (2019). The C* indicates that there is significant overlap of SVOC and IVOC detection between the two instruments (Fig 4c). Whilst the iodide ionisation scheme detected HOM, it did not detect any ELVOC (extremely low volatile compounds) and very little LVOC (low volatile compounds), detecting instead mainly IVOC (intermediate volatile compounds), SVOC (semi volatile compounds) and some VOC (Fig 4c). This is in contrast to the nitrate scheme which detected mainly ELVOC, SVOC and some IVOC, although less than the iodide. This highlights that sampling with both nitrate and iodide schemes captures a large range of gas phase oxidation products, as has been shown in other systems (e.g. Riva *et al.*, 2019).

3.2. Mechanistic investigation

Nitrate CIMS is routinely used to detect HOM, but iodide CIMS is also able to detect high mass compounds (Mohr *et al.,* 2019). To test the extent to which the iodide CIMS is able to detect HOM that could potentially originate from autoxidative processes, a number of theoretically suggested formulae based on the autoxidation mechanism with propagation and termination steps were devised and then searched for within the spectra. The applied mechanism includes the benzene oxidation scheme from the MCM with two additional autoxidation steps added in. It consists of autoxidative intra-molecular hydrogen shifts from the carbon backbone to a peroxy radical group forming a hydroperoxide group, followed by O_2 addition to form a new peroxy radical (Fig 1). The peroxy radical groups were terminated to hydroxyl, peroxyl, nitrate or peroxy nitrate groups, or reduced to form the alkoxy equivalent which then terminates to a carbonyl group or a nitro group (isomeric with nitrite). This was repeated for phenol and catechol precursors as products of subsequent OH attack (Garmash *et al.*, 2020). To reduce complexity, this subsequent OH attack is only considered at the beginning of the mechanism. This provides a total of 53 individual oxidation products with 21 unique formula. All the suggestions of potential mechanistic routes to formation are speculative and set against the mechanistic paradigm laid out here.

We observe 14 and 21 individual deprotonated and adduct signals in the low and high NO_x spectra that correspond to 9 and 11 unique formula respectively. These 9 and 11 unique formula correspond to a maximum of 27 and 33 individual oxidation products (Table S1). At least one signal (adduct or deprotonated) for all theoretic CHO products is observed in the low NO_x case apart from $C_6H_8O_9$ and $C_6H_8O_{10}$, although these are observed in the nitrate spectrum. No derived CHON are observed in the low NO_x case indicating that the incorporation of nitrogen into compounds observed under these conditions occurs at a later point. All three are found in the low NO_x case and $C_6H_8O_7$ and $C_6H_8O_8$ are found in the high NO_x case. $C_6H_8O_8$ is an exclusively second generation autoxidation product that has been observed previously in benzene oxidation studies (Molteni *et al.*, 2018). $C_6H_8O_9$ and $C_6H_8O_{10}$ are not observed in the high NO_x case. $C_6H_7NO_4$, $C_6H_7NO_6$, $C_6H_7NO_7$, are the only NO_x containing species observed in the high NO_x case. The formation of $C_6H_7NO_4$ has two mechanistic routes, the nitration of the initial hydroxy benzene peroxy radical or the addition of a peroxy nitrate group to the phenol, whereas $C_6H_7NO_6$, $C_6H_7NO_7$ have numerous routes to formation with the only non-autoxidation route being the nitration of phenol and catechol respectively. Exclusively second generation high oxygen content CHON species $C_6H_7NO_8$, $C_6H_7NO_9$, $C_6H_7NO_{10}$, $C_6H_7NO_{11}$ are not observed with iodide but are observed with nitrate. Figure 5 summarises these ions in the mass spectra.

HOM and autoxidation are currently not a common inclusion in chemical box models, although some mechanisms are available (e.g. Weber *et al.*, 2020). Due to its usage and optimisation for HOM detection, nitrate CIMS does not typically provide insight into traditional oxidation chemistry, as its sensitivity to low molecular weight species is poor. In order to assess the traditional oxidation chemistry of this system, we describe which oxidation products from the MCM (Jenkin *et al.*, 2003; Bloss *et al.*, 2005) are detectable by iodide CIMS.

3.2.1. MCM products

The MCM lists 85 multigenerational oxidation products of benzene including important intermediate and radical species (Jenkin *et al.*, 2003; Bloss *et al.*, 2005). The iodide ToF-CIMS detects 19 (~25 %) and 26 (~30 %) of these 85 oxidation products under low and high NO_x conditions (Fig 6). These signals are a mixture of adducts and non-adduct peaks that match the exact masses of the MCM oxidation products to within 20 ppm error. Whilst only 19 and 26 of the species with a formula cited in the MCM are detected, signals increase for 132 and 195 peaks in the mass spectrum under low and high NO_x conditions respectively indicate many more products are formed than are explicitly accounted for. The distributions of the number of detected C, H, O and N broadly follows the available MCM C, H, O and N, for example the number of C_3 and C_5 compounds in this reaction scheme are much fewer than $C_{2,4,6}$ which is reflected proportionally in the number of detected species. This suggests that distributed over the entire mechanism, there is no preference for detection of any specific CHON configurations. A list of all detected species can be found in table S2.

Without calibration, much of the oxidation product descriptions must be either; tentative, when making direct identifications; or broad, and describe only bulk properties. In the absence of direct calibration, we describe the bulk properties of iodide CIMS detected CHO and CHON compounds and group them according to chemical composition criteria in order to present an overall depiction of all detectable oxidation products.

3.3. Iodide CIMS detected CHO and CHON under low and high NO_x conditions

A total of 132 and 195 adduct and deprotonated peaks identified as CHO or CHON in the low and high NO_x experiments respectively using the iodide CIMS of which 126 are common between the experiments (Fig 7). The number of detected compounds is much higher in the high NO_x case compared with the low NO_x case. This is expected as the complexity of the system increases and additional reaction pathways are viable. This is especially true regarding the detection of N containing compounds. As the chamber had a NO_x background of ~ 300 ppt, formation of N-containing compounds still occurred during the low NO_x experiment. Twenty four N-containing products were detected during the low NO_x experiment compared with 70 detected during the high NO_x experiment (20 ppb NO_x) of which 23 were common.

The majority of species detected are C_6 and C_4 compounds (Fig 8a) in both cases. with O_{3-4} also most abundant. The atom distributions (Fig 8a-d) appear very similar, with the largest difference being the number of detected N containing compounds (Fig 8d), where more than twice as many are detected in the high NO_x case. The average carbon and hydrogen atom number for the detected species is marginally higher for the low NO_x case than for the high NO_x case (Fig 8e). This observation is further enhanced when weighting the average composition by signal rather than merely counting detected species. This is consistent with greater fragmentation occurring under higher NO_x conditions and is also reflected in the average masses of the reaction products when signal weighted (Fig 8g). The O:C and H:C ratios are very similar between the two experiments ($H:C_{lowNOx} = 1.34$ and $O:C_{lowNOx} = 0.93$ compared with $H:C_{highNOx} = 1.34$ and $O: C_{highNOx} = 1.02$, Fig 8h) and is reflected in $\overline{OS_C}$, which is marginally higher in the high NO_x case (0.36 vs. 0.42) although the range of possible $\overline{OS_C}$ for both experiments have significant overlap (0.31 - 0.42 for the low NO_x case and 0.28– 0.60 for the high NO_x case, Fig 8h). The small differences in oxidation product characteristics between the two NO_x conditions indicates bulk analysis of all oxidation products is not sensitive enough. In order to better understand the differences between oxidation products from the different NO_x cases, the ions are grouped by preference to formation under high or low NO_x conditions (defined as the regime in which signal enhancement is greatest) and re-analysed (Fig S2). Despite having a very similar average mass, those products that preferentially formed under high NO_x conditions have a lower $\overline{OS_C} < 0.13$ compared to the low NO_x conditions where $\overline{OS_C} \sim 0.39$.

In order to better describe these oxidation products, five different groupings of compounds are used to categorise detected oxidation products. Background species refer to those present in the chamber before oxidation and comprise < 0.05 % of total signal. Compounds of formulae that match species described in the benzene oxidation mechanism of the MCM are denoted MCM and comprise < ~10 % of signal whilst highly oxidised products are identified as species containing 6 or more oxygen atoms and comprise < ~0.3 % of signal. These highly oxidised products can include ring breaking and ring retaining products. The rest of the products are termed remainder and are either ring retaining or ring breaking based on the number of carbon atoms present. Where 6 carbon atoms are present and the double bond equivalent (DBE) equals 4 then the species is ring retaining, and where these criteria are not met, it is defined as a ring breaking product (Mehra *et al.*, 2020). Remaining ring breaking products make up the most of the remaining signal (~90 %) leaving ring retaining products contributing < ~4%.

MCM and ring breaking products are observed to grow continually over the time period of oxidation, whereas highly oxidised and ring retaining products equilibrate and remain flat for the duration of the experiment (Fig 9). This is also true of the high NO_x experiment, although when NO_2 photolysis stops halfway through the oxidation, the growth of signal is diminished and the saw tooth profile less apparent. The MCM and ring breaking groups contain small, oxidised molecules that are near the end of the oxidative chain representing large sink of the carbon in the system and so continually grow. The ring retaining and highly oxidised species reach an equilibrium quickly as they tend to be earlier generation products and so their profiles remain flat.

3.3.1. Ring retention and ring breaking products

In terms of signal, most of the ring retaining products are $O_{1,2,3}$ of which $O_{1,2}$ is dominated by the formation of phenol and catechol. Conversely, O_3 isn't dominated by any one product, but instead comprises of both CHO and CHON products in both NO_x conditions (Fig 10). Although O_{1-7} species are observed in both cases, higher O numbers of 10, 11 and 12 are only visible in the high NO_x case due to the presence of nitrogen groups that can incorporate more oxygen.

For the ring breaking products, the majority of signal can be attributed to the presence of species containing 3 and 4 oxygen atoms, although at lower carbon numbers of 1 and 2 lower oxygen numbers of 1 and 2 become important (Fig 11). The majority of signal for both cases is due to $C_{1,2,3}$ compounds. C_3 compounds show the greatest signal contribution for the largest range of oxygen numbers. This is especially true in the high NO_x case where signal C_3 compounds have a greater contribution from $O_{>4}$. Similarly at higher carbon numbers e.g. 5 and 6, higher oxygen numbers of between 6 and 12 are more readily observed, again where N is incorporated in the high NO_x case a greater inclusion of oxygen is also observed. The form of this organic nitrogen is perturbed throughout the experiment by altering the NO/NO_x fraction by photolysing NO_2. It is stressed that as these values are reported as uncalibrated instrument responses, they cannot be used to directly assess chemical pathways. However they allow for the comparison of product distributions between high and low NO_x conditions in terms of sensitivity to iodide CIMS measurements (Fig 10 and Fig 11).

Descriptions of bulk properties and groupings into large families are a useful method to assess broad trends within the system. However it may be possible to produce less granularity in identified species by looking at specific atomic composition and attempting to infer potential functionality.

3.4. Hierarchical cluster analysis to infer CHON functionality

A four cluster solution was chosen from analysis of the dendrogram (Fig S3) and is sufficient to provide enough detail that can be explained, but not so much that interpretation becomes unclear. Further refinement of clusters greater than 4 offers no more insight in time series behaviour due to oxidation behaviour but rather describes signal delay likely due to gas wall partitioning (Krechmer *et al.*, 2016; Pagonis *et al.*, 2017). This behaviour is still observed in the four cluster solution, however other affects pertaining to chemistry rather than partitioning are more visible at this low cluster number. Therefore the four cluster solution is chosen (Fig 12). See Table S2. for a list of MCM defined products and their assigned clusters.

Cluster 3 and cluster 4 do not display much effect of NO_2 photolysis. Cluster 3 is a slow formation cluster that grows as photo-oxidation begins. This is likely to represent semi-volatile material that partitions to walls and equilibrates with the instrument lines and IMR. Cluster 4 is a background cluster that decays when photo-oxidation begins (TUV on) and recovers when photo-oxidation stops. The background cluster 4 has the lowest number of RNO_x containing members, and the slow growth, semi-volatile cluster 3 has the greatest number (Fig 13c). Cluster 4 contains the greatest number of species with high carbon numbers with a negative $\overline{\mathrm{OS}_C}$. These characteristics are reflected in cluster 3 but to a lesser extent as carbon numbers are smaller and $\overline{\mathrm{OS}_C}$ less negative. It is also notable that cluster 1 products remain at elevated levels in the chamber after all photochemistry has stopped. This again may be indicative of more semi volatile material formed. This is anecdotally corroborated by the higher oxygen and carbon numbers of cluster 1 compared to cluster 2 (Fig 13a). Cluster 2 shares time series features that are similar to clusters 1 and 3. It has the same long range response as cluster 3 but the same short range increase from photo-oxidation as cluster 1. This is reflected in Fig. 13b where cluster 2 overlaps with clusters 1 and 3, which themselves are well separated. Both these clusters have lower average carbon numbers and higher, positive $\overline{\mathrm{OS}_C}$ compared with clusters 3 and 4 (Fig 13b).

Clusters 1 and 2 represent the formation of oxidation products. They increase similarly when photo-oxidation is initiated, however when the NO_2/NO_x ratio is increased, cluster 1 continues to increase but cluster 2 decreases. This suggests cluster 1 products are independent of NO_2/NO_x ratio at these high NO_2 fractions; the growth curve is independent of the decrease in NO concentration, suggesting this cluster is characterised by more reactions of NO_2 and peroxy radicals. Conversely to cluster 1, cluster 2 decreases when the NO_2/NO_x increases suggesting NO is an important route to formation, either from NO addition products or the increased alkoxy radical fraction RO/RO_2, which is supported by cluster 2 products having higher $\overline{OS_C}$ and lower carbon numbers than cluster 1 products.

Both clusters 1 and 2 contain a similar number of RNO and RNO_2 species, but cluster 1 has a greater, odd number of oxygen as RNO_3 and RNO_5, whereas cluster 2 has a greater even number of oxygen in RNO_4 and RNO_6. The inclusion of these groupings in one cluster leads to a lack of them in the other; no RNO_4 or RNO_6 are found in cluster 1 nor is there a large amount of RNO_5 or any RNO_3 in cluster 2.

Ideally, NO and NO_2 addition to peroxy precursors (cluster 1) would produce nitrates and peroxy acyl nitrates (PANs) that have an odd number of oxygens (RNO_3 and RNO_5), and addition to alkoxy precursors (cluster 2) would produce nitro- and nitrite compounds that have an even number of oxygens (RNO_2). This is indeed observed, however in reality this distinction is not so clear cut as OH addition vs abstraction would reverse this. So although these observations are broadly followed, they are not exact resulting in a blurring of RNO_x groupings, especially at higher O numbers (Fig 13c). Both clusters 1 and 2 have the same number of RNO_7 species despite their time series profiles showing a different dependency on the NO_2/NO_x ratio. It is likely that these RNO_7 are structurally different and the oxygen is incorporated into their structures in different ways. For example cluster 1 RNO_7, which are all C_5 and C_6 compounds, may contain more PAN like compounds as these are formed from peroxy acyl radicals and NO_2 addition e.g. to BZEMUCCO3 (MCM), which is the peroxy radical formed from BZEPOXMUC, a first generation ring opening product of benzene, to form BZEMUCPAN ($C_6H_5NO_7$). In contrast, cluster 2 RNO_7 are smaller C_3 and C_4 compounds, which may require the fragmentation of larger organic precursors enhanced by the presence of NO e.g. the unimolecular decomposition of the alkoxy radical MALANHYO to form HCOCOHCO3 and then HCOCOPAN ($C_3H_3NO_7$).

4. Conclusion

Two ToF-CIMS using iodide and nitrate ionisation schemes were deployed at the Jülich plant chamber as part of a series of experiments examining benzene oxidation by OH under high (20 ppb) and low (0.3 ppb) NO_x conditions.

Both ionisation schemes detect benzene oxidation products including highly oxidised organic molecules. Nitrate CIMS detects many C_{12} dimers and a greater number of species with high oxygen number (O_9-O_{11}). This translates to higher $\overline{OS_C}$, especially at higher carbon numbers ($C_{\geq 8}$), and lower C* indicating the detection of ELVOC, SVOC and IVOC. In contrast, the iodide CIMS detects no dimers, but does detect a wider range of monomers and ring breaking products ($C_{\leq 6}$) than the nitrate scheme, with most common oxygen numbers of (O_3-O_4). The $\overline{OS_C}$ of high carbon species is lower, although at lower carbon numbers ($C_{<6}$) $\overline{OS_C}$ between the two ionisation schemes broadly agree due to the increased likelihood of measuring the same species, rather than isomers. The corresponding C* measured by the iodide CIMS suggests no ELVOC was detected, but more SVOC, IVOC and some VOC were measured when compared to the nitrate CIMS. Thus the two ionisation schemes cover a large range of volatilities.

CHO species (132) and CHON species (195) are detected in the low and high NO_x experiments, respectively. Of these 126 are common. In both cases these are mostly C_4 and C_6 compounds. A greater number of oxidation products are measured in the high NO_x case, including 70 N containing compounds compared to 24 in the low NOx case, of which all but one are common. Splitting oxidation products into five categories, the contribution to signal increases sequentially from background, highly oxidised products, ring retaining, MCM, and ring breaking. The signal assigned to MCM products represents between ¼ and ⅓ of the 85 listed multigenerational oxidation products detected under low and high NO_x conditions and are proportionally distributed across all carbon numbers. Highly oxidised and ring retaining products equilibrate quickly within the system and remain throughout the experiments, whereas MCM and ring breaking products continue to grow throughout the experiments. Highly oxidised and ring retaining products are earlier generation products which form quickly and equilibrate as loss and formation processes equalise. MCM and ring breaking products contain smaller, more oxidised molecules that are further down the oxidation chain and represent the largest destination of carbon within the system. Signal from ring retaining products is dominated by phenol (O_1) and catechol (O_2) whereas O_3 compounds comprise a number of different species. Ring breaking products are dominated by C_1, C_2 and C_3 compounds with similar oxygen numbers. C_3 compounds show the greatest variability of oxygen atom number. For both retention and breaking products, high O numbers of up to 7 are identified, however in the high NO_x case where incorporation of RNO_x is greater, higher O numbers of 10, 11 and 12 are observed. Within the context of the theoretical mechanistic investigation (section 3.3), iodide ionisation is able to detect 27 and 33 species belonging to potential autoxidation reaction pathways. These detected species include one previously observed, exclusively second generation autoxidation product, $C_6H_8O_8$, and all its derived 1st generation autoxidation products. However, it is noted that only two of these first generation product steps ($C_6H_8O_6$, $C_6H_8O_7$) are formed exclusively through autoxidation whilst the rest have other routes to formation. Higher oxygen content products $C_6H_8O_9$ and $C_6H_8O_{10}$ are not observed in either NO_x case by iodide but are observed with the nitrate CIMS.

Clustering the time series in the high NO_x experiment into four clusters distinguishes two clusters that contain products formed from photo-oxidation. One of these clusters (cluster 1) is independent of the NO_2/NO_x ratio whereas a second cluster (cluster 2) decreases as a result of NO dependent formation, either through addition and/or an increased RO/RO_2 fraction. Cluster 2 has higher $\overline{OS_C}$ and lower carbon numbers than cluster 1 suggesting it consists of more oxidised and fragmented compounds consistent with an increased RO/RO_2. Cluster 2 contains RNO_4 and RNO_6 but no RNO_3 and little RNO_5 whereas the opposite is true for cluster 1. This somewhat agrees with theoretical RNO_x product distributions as NO_x addition to alkoxy radicals (cluster 2) is more likely to produce even oxygen content RNO_x (through the formation of nitrites and nitro compounds), and odd oxygen RNO_x through addition to peroxy radicals (cluster 1, such as nitrates and PANs). For species with larger oxygen content e.g. RNO_7 which is detected in both clusters, the carbon number is lower for cluster 2 ($C_{3,4}$) compared to cluster 1 ($C_{5,6}$) indicating more fragmentation has occurred, again implying a greater contribution from the alkoxy channel. It is noted that the effect of OH addition, rather than H abstraction as the initiation step to the reaction, will reverse this pattern, and along with other unimolecular rearrangements, may explain some of the RNO_x cluster variability observed. This methodology used in conjunction with an internal calibration procedure such as voltage scanning (Lopez-Hilfiker *et al.*, 2015) could then be used to quantitatively describe shifts in CHON composition as a function of NO/NO_x and further investigate the relative importance of isomers and their formation pathways to a mass spectrometric signal.

Contributions

MP analysed nitrate and iodide ToF-CIMS data and wrote the manuscript. OG analysed nitrate ToF-CIMS data and provided peaklist data. TJB and MLB operated the iodide CIMS. CJP, GM, HC, TFM, DES, AM, SDW and AB contributed to iodide CIMS analysis and manuscript development. CJP and GM led the development of the experiments presented here. TFM, AKS, CJP, MH, GM, ÅH designed the experiments. SK, IP, SS, RT, EK, DZ, JW operated the nitrate CIMS and performed the experiments.

Acknowledgements

This work was conducted during a PhD study supported by the Natural Environment Research Council (NERC) EAO Doctoral Training Partnership and is fully-funded by NERC whose support is gratefully acknowledged (Grant ref no. NE/L002469/1).The study was funded by European Research Council grant 638703 and supported by Doctoral School in Atmospheric Sciences at the University of Helsinki (ATM-DP). This work was supported by The Academy of Finland (grant numbers 317380 and 320094) and the Swedish Research Council (grant number 2014-5332). Å.M.H. acknowledges Formas (grant number 214-2013-1430) and Vinnova Sweden’s Innovation Agency (grant number 2013-03058), including support for her research stay at Forschungszentrum Jülich. Part of the research in this study was performed at the Jet Propulsion Laboratory, California Institute of Technology, under a contract with the National Aeronautics and Space Administration.

Competing Interests

The authors declare no competing interests.

Data Availability

Data is available on request.

References

Archibald, A. T. *et al.* (2015) ‘Long-term high frequency measurements of ethane, benzene and methyl chloride at Ragged Point, Barbados: Identification of long-range transport events’, *Elementa: Science of the Anthropocene*, 3, p. 000068. doi: 10.12952/journal.elementa.000068.

Atkinson, R. (2000) ‘Atmospheric chemistry of VOCs and NOx’, *Atmospheric Environment*, 34(12–14), pp. 2063–2101. doi: http://dx.doi.org/10.1016/S1352-2310(99)00460-4.

Atkinson, R. and Arey, J. (2007) ‘Mechanisms of the gas-phase reactions of aromatic hydrocarbons and PAHs with OH and NO3 Radicals’, *Polycyclic Aromatic Compounds*, 27(1), pp. 15–40. doi: 10.1080/10406630601134243.

Berndt, T. *et al.* (2016) ‘Hydroxyl radical-induced formation of highly oxidized organic compounds’, *Nature Communications*, 7(May), p. 13677. doi: 10.1038/ncomms13677.

Bianchi, F. *et al.* (2019) ‘Highly Oxygenated Organic Molecules (HOM) from Gas-Phase Autoxidation Involving Peroxy Radicals: A Key Contributor to Atmospheric Aerosol’, *Chemical Reviews*, 119(6), pp. 3472–3509. doi: 10.1021/acs.chemrev.8b00395.

Bird, M. G. *et al.* (2010) ‘BENZENE 2009-Health effects and mechanisms of bone marrow toxicity: Implications for t-AML and the mode of action framework’, *Chemico-Biological Interactions*. Elsevier Ireland Ltd, 184(1–2), pp. 3–6. doi: 10.1016/j.cbi.2009.12.001.

Bloss, C. *et al.* (2005) ‘Development of a detailed chemical mechanism (MCMv3.1) for the atmospheric oxidation of aromatic hydrocarbons’, *Atmospheric Chemistry and Physics*, 5(3), pp. 641–664. doi: 10.5194/acp-5-641-2005.

Borrás, E. and Tortajada-Genaro, L. A. (2012) ‘Secondary organic aerosol formation from the photo-oxidation of benzene’, *Atmospheric Environment*. Elsevier Ltd, 47(x), pp. 154–163. doi: 10.1016/j.atmosenv.2011.11.020.

Buchholz, A. *et al.* (2019) ‘Deconvolution of FIGAERO-CIMS thermal desorption profiles using positive matrix factorisation to identify chemical and physical processes during particle evaporation’, *Atmospheric Chemistry and Physics*, pp. 1–36. doi: 10.5194/acp-2019-926.

Chhabra, P. S. *et al.* (2015) ‘Application of high-resolution time-of-flight chemical ionization mass spectrometry measurements to estimate volatility distributions of α-pinene and naphthalene oxidation products’, *Atmospheric Measurement Techniques*, 8(1), pp. 1–18. doi: 10.5194/amt-8-1-2015.

Creasey, D. J., Heard, D. E. and Lee, J. D. (2002) ‘Eastern Atlantic Spring Experiment 1997 (EASE97) 1. Measurements of OH and HO2 concentrations at Mace Head, Ireland’, *Journal of Geophysical Research: Atmospheres*, 107(D10), p. ACH 3-1-ACH 3-15. doi: 10.1029/2001JD000892.

Ehn, M. *et al.* (2014) ‘A large source of low-volatility secondary organic aerosol’, *Nature*, 506(7489), pp. 476–479. doi: 10.1038/nature13032.

Fally, S., Carleer, M. and Vandaele, A. C. (2009) ‘UV Fourier transform absorption cross sections of benzene, toluene, meta-, ortho-, and para-xylene’, *Journal of Quantitative Spectroscopy and Radiative Transfer*, 110(9–10), pp. 766–782. doi: 10.1016/j.jqsrt.2008.11.014.

Garmash, O. *et al.* (2020) ‘Multi-generation OH oxidation as a source for highly oxygenated organic molecules from aromatics’, *Atmospheric Chemistry and Physics*, 20(1), pp. 515–537. doi: 10.5194/acp-20-515-2020.

Gentner, D. R. *et al.* (2012) ‘Elucidating secondary organic aerosol from diesel and gasoline vehicles through detailed characterization of organic carbon emissions’, *Proceedings of the National Academy of Sciences*, 109(45), pp. 18318–18323. doi: 10.1073/pnas.1212272109/-/DCSupplemental.www.pnas.org/cgi/doi/10.1073/pnas.1212272109.

Glowacki, D. R., Wang, L. and Pilling, M. J. (2009) ‘Evidence of formation of bicyclic species in the early stages of atmospheric benzene oxidation’, *Journal of Physical Chemistry A*, 113(18), pp. 5385–5396. doi: 10.1021/jp9001466.

Guo, Y. *et al.* (2018) ‘Treatment of real benzene dye intermediates wastewater by the Fenton method: characteristics and multi-response optimization’, *RSC Advances*. Royal Society of Chemistry, 8(1), pp. 80–90. doi: 10.1039/C7RA09404C.

Henze, D. K. *et al.* (2007) ‘Global modeling of secondary organic aerosol formation from aromatic hydrocarbons: high- vs low-yield pathways’, *Atmospheric Chemistry and Physics Discussions*, 7(5), pp. 14569–14601. doi: 10.5194/acpd-7-14569-2007.

Hoyt, D. and Raun, L. H. (2015) ‘Measured and estimated benzene and volatile organic carbon (VOC) emissions at a major U.S. refinery/chemical plant: Comparison and prioritization’, *Journal of the Air and Waste Management Association*. Taylor & Francis, 65(8), pp. 1020–1031. doi: 10.1080/10962247.2015.1058304.

Isaacman-Vanwertz, G. *et al.* (2018) ‘Chemical evolution of atmospheric organic carbon over multiple generations of oxidation’, *Nature Chemistry*. Springer US, 10(4), pp. 462–468. doi: 10.1038/s41557-018-0002-2.

Isaacman-VanWertz, G. *et al.* (2017) ‘Using advanced mass spectrometry techniques to fully characterize atmospheric organic carbon: current capabilities and remaining gaps’, *Faraday Discuss.*, 200, pp. 579–598. doi: 10.1039/C7FD00021A.

Isokääntä, S. *et al.* (2020) ‘Comparison of dimension reduction techniques in the analysis of mass spectrometry data’, *Atmospheric Measurement Techniques*, 13(6), pp. 2995–3022. doi: 10.5194/amt-13-2995-2020.

IUPAC (2008) *IUPAC Task Group on Atmospheric Chemical Kinetic Data Evaluation – Data Sheet HOx _ AROM1*, *IUPAC*. Available at: http://iupac.pole-ether.fr/htdocs/datasheets/pdf/HOx_AROM1_HO_benzene.pdf (Accessed: 12 October 2020).

Jenkin, M. E. *et al.* (2003) ‘Protocol for the development of the Master Chemical Mechanism, MCM v3 (Part B): Tropospheric degradation of aromatic volatile organic compounds’, *Atmospheric Chemistry and Physics*, 3(1), pp. 181–193. doi: 10.5194/acp-3-181-2003.

Johnson, D. *et al.* (2005) ‘Simulating the Formation of Secondary Organic Aerosol from the Photooxidation of Aromatic Hydrocarbons’, *Environmental Chemistry*, 2(1), p. 35. doi: 10.1071/EN04079.

Kamps, R. *et al.* (1993) ‘Photooxidation of exhaust pollutants. I. Degradation efficiencies, quantum yields and products of benzene photooxidation’, *Chemosphere*, 27(11), pp. 2127–2142. doi: 10.1016/0045-6535(93)90125-O.

Knote, C. *et al.* (2014) ‘Simulation of semi-explicit mechanisms of SOA formation from glyoxal in aerosol in a 3-D model’, *Atmospheric Chemistry and Physics*, 14(12), pp. 6213–6239. doi: 10.5194/acp-14-6213-2014.

Koss, A. R. *et al.* (2020) ‘Dimensionality-reduction techniques for complex mass spectrometric datasets: application to laboratory atmospheric organic oxidation experiments’, *Atmospheric Chemistry and Physics*, 20(2), pp. 1021–1041. doi: 10.5194/acp-20-1021-2020.

Krechmer, J. E. *et al.* (2016) ‘Quantification of Gas-Wall Partitioning in Teflon Environmental Chambers Using Rapid Bursts of Low-Volatility Oxidized Species Generated in Situ’, *Environmental Science and Technology*, 50(11), pp. 5757–5765. doi: 10.1021/acs.est.6b00606.

Kroll, J. H. *et al.* (2011) ‘Carbon oxidation state as a metric for describing the chemistry of atmospheric organic aerosol’, *Nature Chemistry*, 3(2), pp. 133–139. doi: 10.1038/nchem.948.

Lopez-Hilfiker, F. D. *et al.* (2015) ‘Constraining the sensitivity of iodide adduct chemical ionization mass spectrometry to multifunctional organic molecules using the collision limit and thermodynamic stability of iodide ion adducts’, *Atmospheric Measurement Techniques Discussions*, 8(10), pp. 10875–10896. doi: 10.5194/amtd-8-10875-2015.

Mehra, A. *et al.* (2020) ‘Evaluation of the Chemical Composition of Gas and Particle Phase Products of Aromatic Oxidation’, *Atmospheric Chemistry and Physics*, (March), pp. 1–24. doi: 10.5194/acp-2020-161.

Mentel, T. F. *et al.* (2009) ‘Photochemical production of aerosols from real plant emissions’, *Atmospheric Chemistry and Physics*, 9(13), pp. 4387–4406. doi: 10.5194/acp-9-4387-2009.

Mentel, T. F. *et al.* (2015) ‘Formation of highly oxidized multifunctional compounds: autoxidation of peroxy radicals formed in the ozonolysis of alkenes – deduced from structure–product relationships’, *Atmospheric Chemistry and Physics*, 15(12), pp. 6745–6765. doi: 10.5194/acp-15-6745-2015.

Misztal, P. K. *et al.* (2015) ‘Atmospheric benzenoid emissions from plants rival those from fossil fuels’, *Scientific Reports*, 5(June), pp. 1–10. doi: 10.1038/srep12064.

Mohr, C. *et al.* (2019) ‘Molecular identification of organic vapors driving atmospheric nanoparticle growth’, *Nature Communications*, 10(1), pp. 1–7. doi: 10.1038/s41467-019-12473-2.

Molteni, U. *et al.* (2018) ‘Formation of highly oxygenated organic molecules from aromatic compounds’, *Atmospheric Chemistry and Physics*, 18(3), pp. 1909–1921. doi: 10.5194/acp-18-1909-2018.

Ng, N. L. *et al.* (2007) ‘Secondary organic aerosol formation from m-xylene, toluene, and benzene’, *Atmospheric Chemistry and Physics*, 7(14), pp. 3909–3922. doi: 10.5194/acp-7-3909-2007.

Nguyen, T. B. *et al.* (2015) ‘Rapid deposition of oxidized biogenic compounds to a temperate forest’, *Proceedings of the National Academy of Sciences*, 112(5), pp. E392–E401. doi: 10.1073/pnas.1418702112.

O’Brien, R. J. *et al.* (1983) ‘Carbon Balances in Simulated Atmospheric Reactions: Aromatic Hydrocarbons’, *Environmental Science and Technology*, 17(3), pp. 183–186. doi: 10.1021/es00109a013.

Oyoroko, E. and Ogamba, E. N. (2017) ‘Effects of detergent containing linear alkyl benzene sulphonate on behavioural response of Heterobranchus bidorsalis , Clarias gariepinus and Heteroclarias’, *Biotechnological Research*, 3(3), pp. 59–64. doi: 10.31304.

Pagonis, D. *et al.* (2017) ‘Effects of gas-wall partitioning in Teflon tubing and instrumentation on time-resolved measurements of gas-phase organic compounds’, *Atmospheric Measurement Techniques*, 10(12), pp. 4687–4696. doi: 10.5194/amt-10-4687-2017.

Praske, E. *et al.* (2018) ‘Atmospheric autoxidation is increasingly important in urban and suburban North America’, *Proceedings of the National Academy of Sciences*, 115(1), pp. 64–69. doi: 10.1073/pnas.1715540115.

Priestley, M. *et al.* (2018) ‘Observations of Isocyanate, Amide, Nitrate, and Nitro Compounds From an Anthropogenic Biomass Burning Event Using a ToF-CIMS’, *Journal of Geophysical Research: Atmospheres*, (2), pp. 1–26. doi: 10.1002/2017JD027316.

Pye, H. O. T. *et al.* (2019) ‘Anthropogenic enhancements to production of highly oxygenated molecules from autoxidation’, *Proceedings of the National Academy of Sciences of the United States of America*, 116(14), pp. 6641–6646. doi: 10.1073/pnas.1810774116.

Rissanen, M. P. *et al.* (2014) ‘The formation of highly oxidized multifunctional products in the ozonolysis of cyclohexene’, *Journal of the American Chemical Society*, 136(44), pp. 15596–15606. doi: 10.1021/ja507146s.

Riva, M. *et al.* (2019) ‘Evaluating the performance of five different chemical ionization techniques for detecting gaseous oxygenated organic species’, *Atmospheric Measurement Techniques*, 12(4), pp. 2403–2421. doi: 10.5194/amt-12-2403-2019.

Rodriguez, P. G. *et al.* (2018) ‘Thermochemical stability and friction properties of soft organosilica networks for solid lubrication’, *Materials*, 11(2), pp. 1–12. doi: 10.3390/ma11020180.

Ruchirawat, M. *et al.* (2005) ‘Measurement of genotoxic air pollutant exposures in street vendors and school children in and near Bangkok’, *Toxicology and Applied Pharmacology*, 206(2), pp. 207–214. doi: 10.1016/j.taap.2004.11.025.

Ruchirawat, M. *et al.* (2007) ‘Assessment of potential cancer risk in children exposed to urban air pollution in Bangkok, Thailand’, *Toxicology Letters*, 168(3), pp. 200–209. doi: 10.1016/j.toxlet.2006.09.013.

Sarrafzadeh, M. *et al.* (2016) ‘Impact of NOx and OH on secondary organic aerosol formation from β-pinene photooxidation’, *Atmospheric Chemistry and Physics*, 16(17), pp. 11237–11248. doi: 10.5194/acp-16-11237-2016.

Saunders, S. M. *et al.* (2003) ‘Protocol for the development of the Master Chemical Mechanism, MCM v3 (Part A): tropospheric degradation of non-aromatic volatile organic compounds’, *Atmos. Chem. Phys.* Copernicus

Publications, 3(1), pp. 161–180. doi: 10.5194/acp-3-161-2003.

Sekimoto, K. *et al.* (2018) ‘High- and low-temperature pyrolysis profiles describe volatile organic compound emissions from western US wildfire fuels’, *Atmospheric Chemistry and Physics*, 18(13), pp. 9263–9281. doi: 10.5194/acp-18-9263-2018.

Snyder, R., Kocsis, J. J. and Drew, R. (1975) ‘Current concepts of chronic benzene toxicity’, *Critical Reviews in Toxicology*, 3(3), pp. 265–288. doi: 10.3109/10408447509079860.

Stark, H. *et al.* (2015) ‘Methods to extract molecular and bulk chemical information from series of complex mass spectra with limited mass resolution’, *International Journal of Mass Spectrometry*. Elsevier B.V., 389, pp. 26–38. doi: 10.1016/j.ijms.2015.08.011.

Stirnweis, L. *et al.* (2017) ‘Assessing the influence of NOx concentrations and relative humidity on secondary organic aerosol yields from α-pinene photo-oxidation through smog chamber experiments and modelling calculations’, *Atmospheric Chemistry and Physics*, 17(8), pp. 5035–5061. doi: 10.5194/acp-17-5035-2017.

Surratt, J. D. *et al.* (2006) ‘Chemical Composition of Secondary Organic Aerosol Formed from the Photooxidation of Isoprene’, *The Journal of Physical Chemistry A*, 110(31), pp. 9665–9690. doi: 10.1021/jp061734m.

Surratt, J. D. *et al.* (2010) ‘Reactive intermediates revealed in secondary organic aerosol formation from isoprene’, *Proceedings of the National Academy of Sciences*, 107(15), pp. 6640–6645. doi: 10.1073/pnas.0911114107.

Tsiligiannis, E. *et al.* (2019) ‘Effect of NOx on 1,3,5-trimethylbenzene (TMB) oxidation product distribution and particle formation’, *Atmospheric Chemistry and Physics Discussions*, (x), pp. 1–18. doi: 10.5194/acp-2019-395.

Verma, D. K. and Des Tombe, K. (2002) ‘Benzene in gasoline and crude oil: Occupational and environmental implications’, *American Industrial Hygiene Association Journal*, 63(2), pp. 225–230. doi: 10.1080/15428110208984708.

Volkamer, R. *et al.* (2002) ‘OH-initiated oxidation of benzene’, *Physical Chemistry Chemical Physics*, 4(9), pp. 1598–1610. doi: 10.1039/b108747a.

Wang, S. *et al.* (2017) ‘Formation of Highly Oxidized Radicals and Multifunctional Products from the Atmospheric Oxidation of Alkylbenzenes’, *Environmental Science and Technology*, 51(15), pp. 8442–8449. doi: 10.1021/acs.est.7b02374.

Wang, T. *et al.* (2014) ‘Benzene homologues in environmental matrixes from a pesticide chemical region in China: Occurrence, health risk and management’, *Ecotoxicology and Environmental Safety*, 104(1), pp. 357–364. doi: 10.1016/j.ecoenv.2014.01.035.

Wang, Y. *et al.* (2020) ‘Oxygenated products formed from OH-initiated reactions of trimethylbenzene: Autoxidation and accretion’, *Atmospheric Chemistry and Physics*, (March), pp. 1–32. doi: 10.5194/acp-2020-165.

Weber, J. *et al.* (2020) ‘CRI-HOM: A novel chemical mechanism for simulating highly oxygenated organic molecules (HOMs) in global chemistry–aerosol–climate models’, *Atmospheric Chemistry and Physics*, 20(18), pp. 10889–10910. doi: 10.5194/acp-20-10889-2020.

Wildt, J. *et al.* (2014) ‘Suppression of new particle formation from monoterpene oxidation by NOx’, *Atmospheric Chemistry and Physics*, 14(6), pp. 2789–2804. doi: 10.5194/acp-14-2789-2014.

Zaytsev, A. *et al.* (2019) ‘Mechanistic Study of Formation of Ring-retaining and Ring-opening Products from Oxidation of Aromatic Compounds under Urban Atmospheric Conditions’, *Atmospheric Chemistry and Physics Discussions*, pp. 1–24. doi: 10.5194/acp-2019-666.

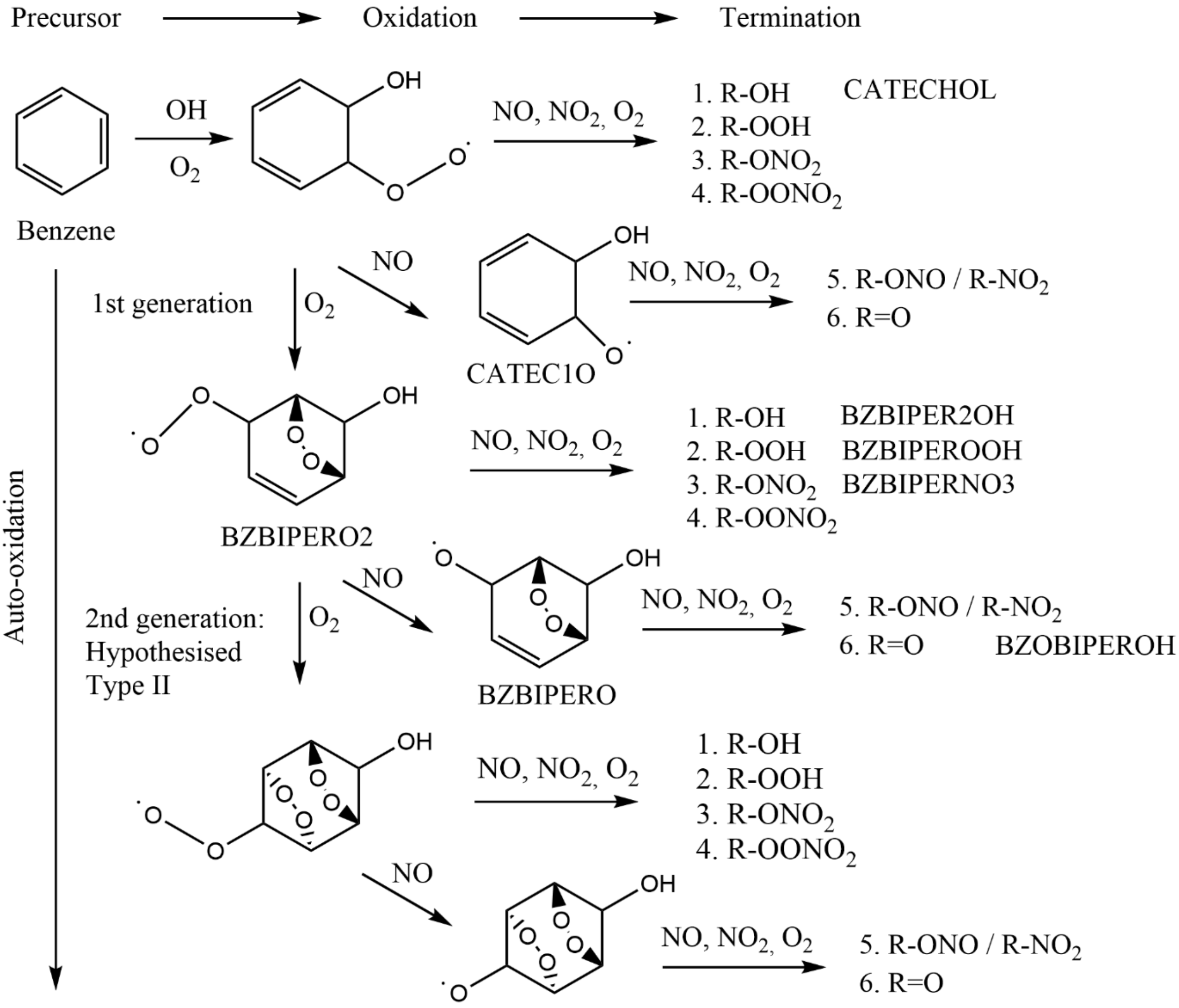

Figure 1. Reaction scheme of benzene oxidation by OH with proposed di-bridged species adapted from Molteni *et al.*, (2018). Species present in the MCM are labelled.

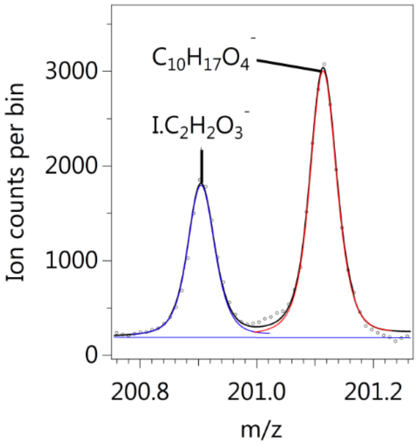

Figure 2. Example of peak separation between an iodide adduct $I.C_2H_2O_3^-$ and deprotonated signal $C_{10}H_{17}O_4^-$ detected during background measurements before the low NO_x experiment.

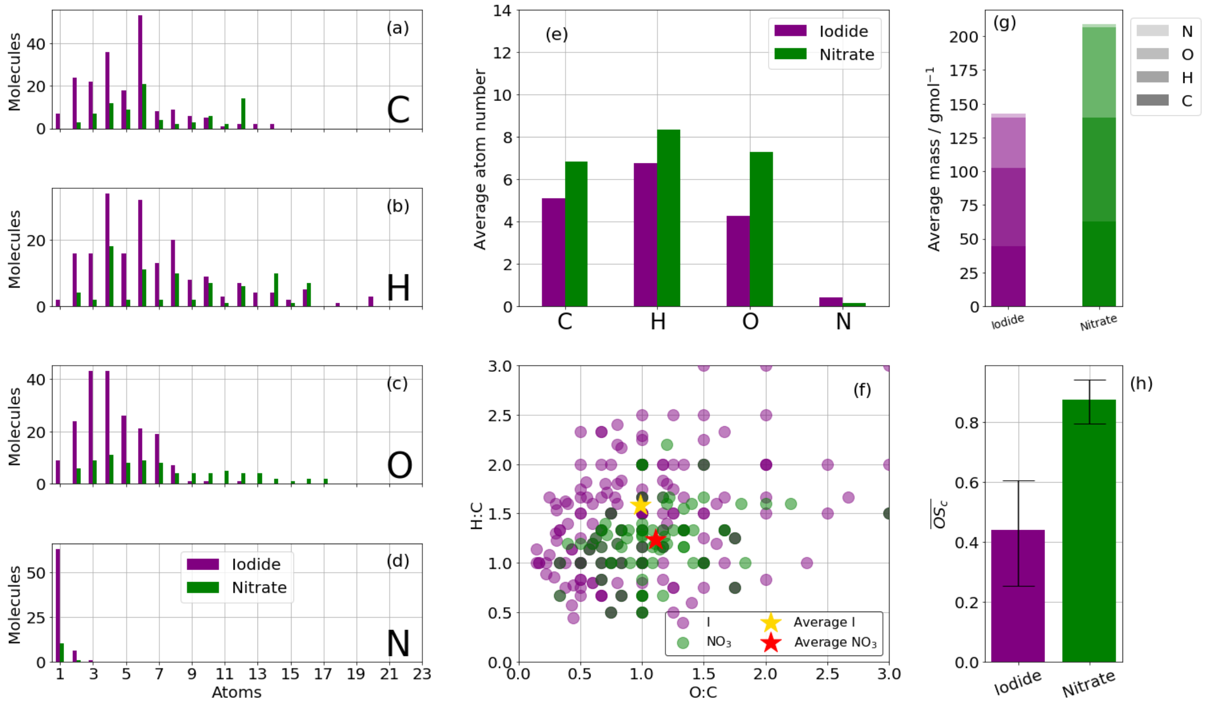

Figure 3. Summary of CHO and CHON statistics of detected oxidation products during the high (20 ppb) NO_x benzene oxidation for iodide (purple) and nitrate (green) ionisation schemes. (a, b, c, d.) Frequency distributions of the atoms C, H, O and N for the detected oxidation products. (e) Average number of atoms per detected oxidation product split into C, H, O and N. (f) Van Krevelen diagram (O:C vs H:C). (g) The average mass of a detected oxidation product detected by iodide and nitrate ionisation. (h) The average carbon oxidation state $\overline{OS_C}$ of oxidation products detected by iodide and nitrate ionisation. Limits represent minimum and maximum $\overline{OS_C}$ as a function of minimum and maximum OS_N, see section 2.3.

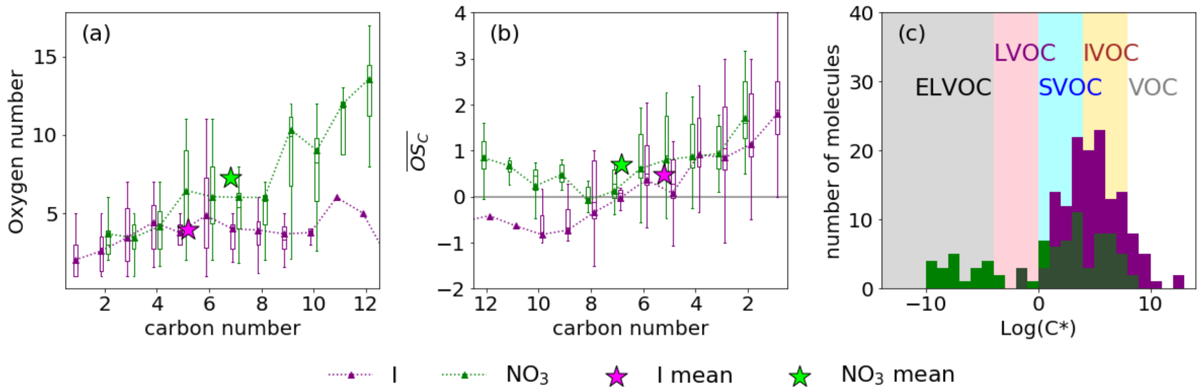

Figure 4. Comparison of organic oxidation products from the iodide (purple) and nitrate (green) ionisation schemes. (a) carbon number vs oxygen number. (b) average carbon oxidation state ($\overline{OS_C}$) vs carbon number. (c) Saturation concentration (C*) based on Mohr *et al.* (2019).

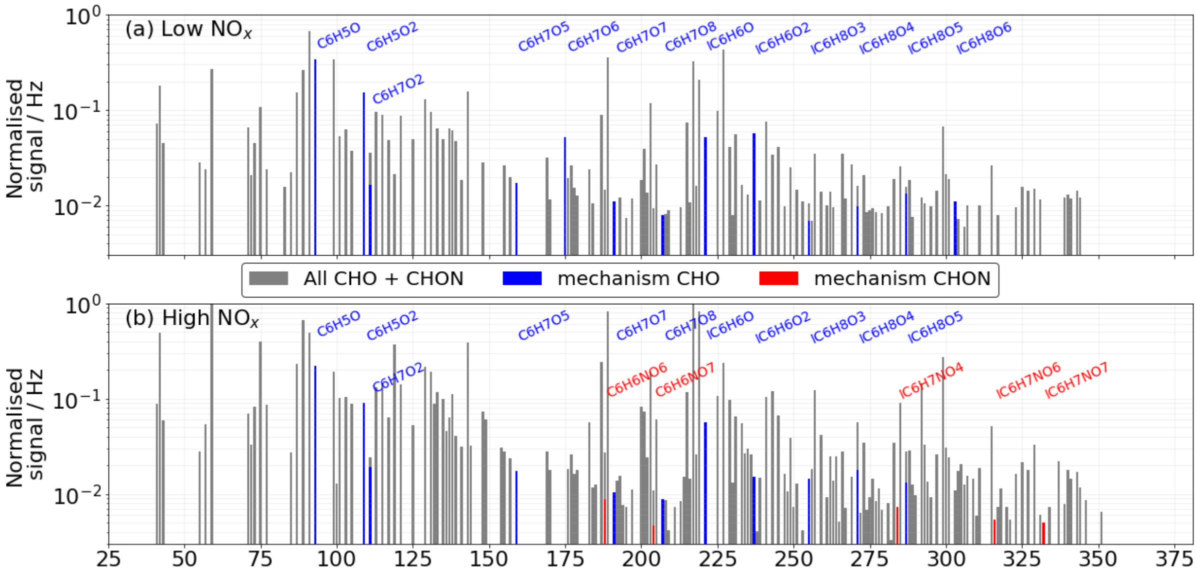

Figure 5. Unit mass spectra of (a) low NO$_x$ and (b) high NO$_x$ experiments from the Iodide CIMS. Detected ions from the mechanism are highlighted as CHO (blue) or CHON (red).

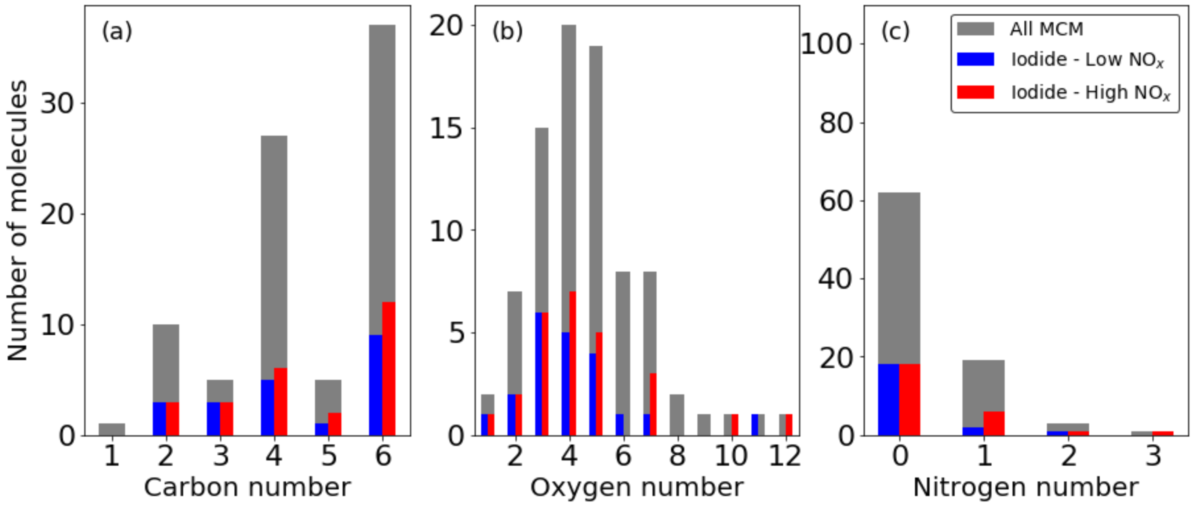

Figure 6. Fraction of ions observed from the MCM in the high and low NO$_x$ experiments expressed as number of molecules containing atom numbers for (a) carbon, (b) oxygen and (c) nitrogen.

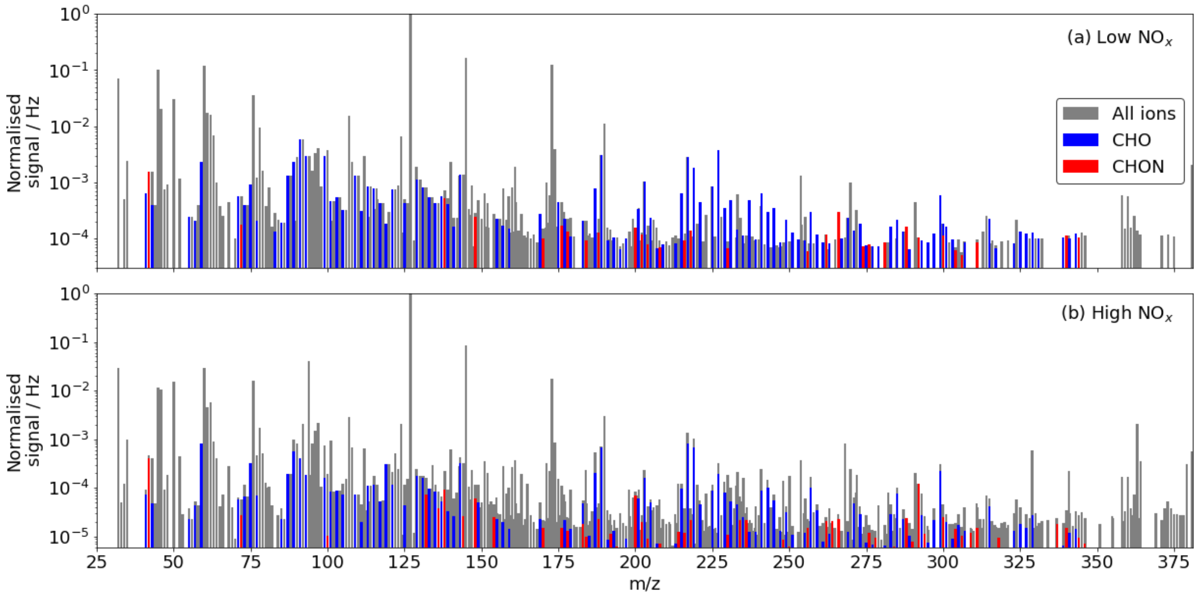

Figure 7. (a) Unit mass spectrum during benzene oxidation by OH under (a) low NO$_x$ conditions and (b) under high NO$_x$ conditions from the iodide CIMS. Identified CHO and CHON compounds are highlighted.

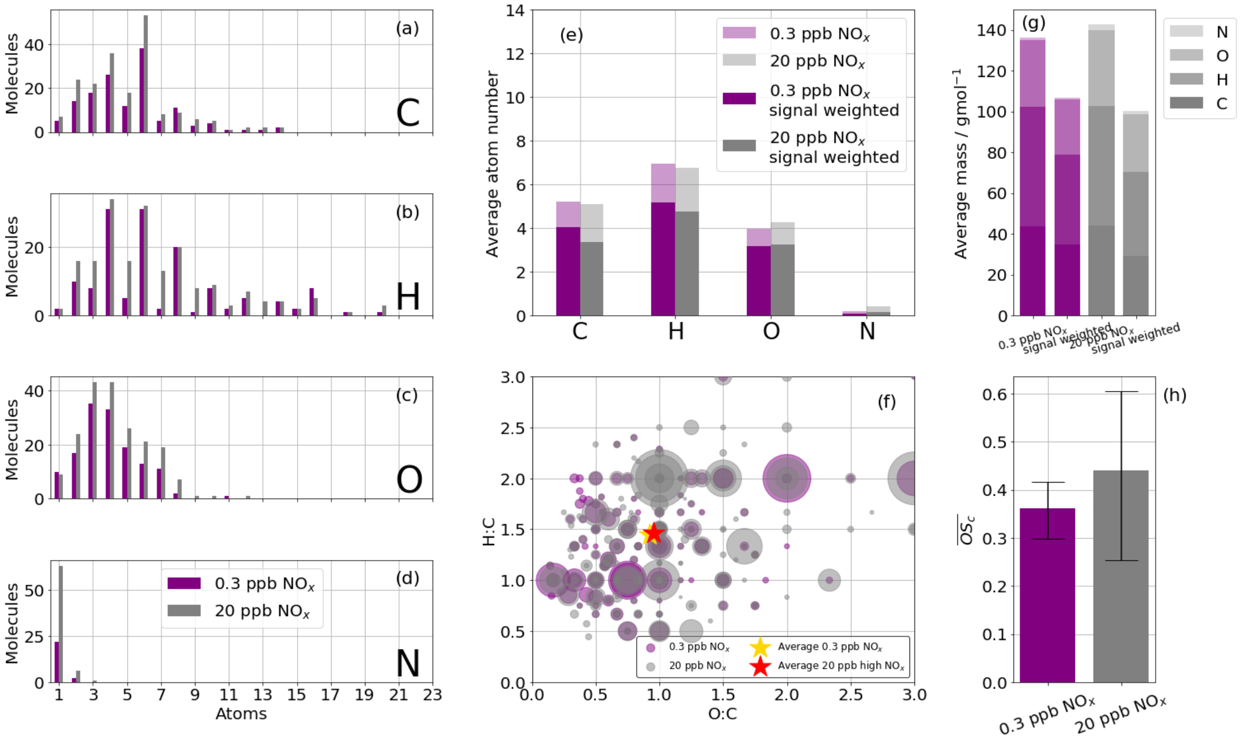

Figure 8. Summary of CHO and CHON statistics of detected oxidation products during high (20 ppb, grey) and low (0.3 ppb, purple) NO$_x$ benzene oxidation with the iodide ionisation scheme. (a, b, c, d.) Frequency distributions of the atoms C, H, O and N for the detected oxidation products. (e.) The average number of atoms per detected oxidation product split into C, H, O and N atoms, also shown is signal weighted average atom number. (f.) Van Krevelen diagram (O:C vs H:C) sized by signal. (g.) The average mass of a detected oxidation product for high and low NO$_x$ conditions, also shown signal weighted average masses. (h.) The mean, average carbon oxidation state ($\overline{OS_C}$) of the detected oxidation products for high and low NO$_x$ conditions. Limits represent minimum and maximum OS_C as a function of minimum and maximum OS_N, see section 2.3.

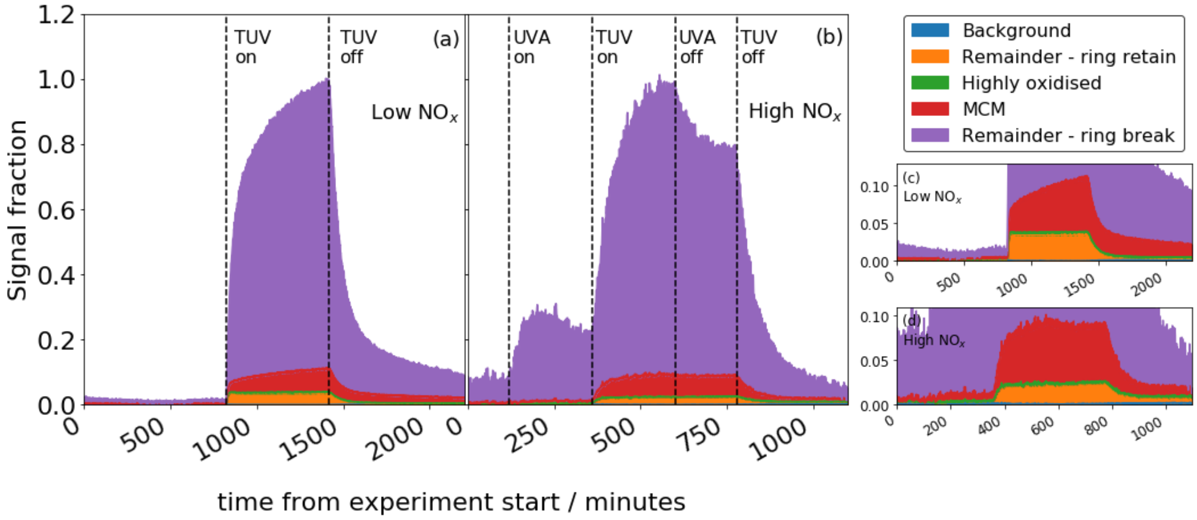

Figure 9. Total signal from CHON + CHO compounds for the low NO$_x$ (a) and high NO$_x$ (b) experiments. (c) and (d) show the same data in (a) and (b) with a reduced y scale; y and x scale have the same units.

795

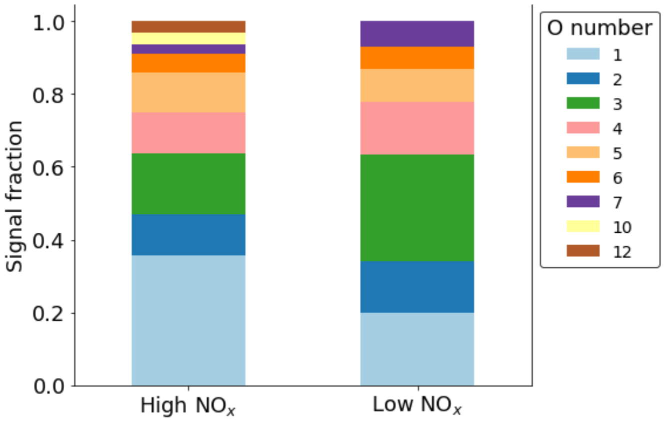

Figure 10. Normalised signal fraction of ring retaining products under high and low NO$_x$ conditions. Signal for phenol and catechol dominate for both conditions and make up the O_1 and O_2 fractions.

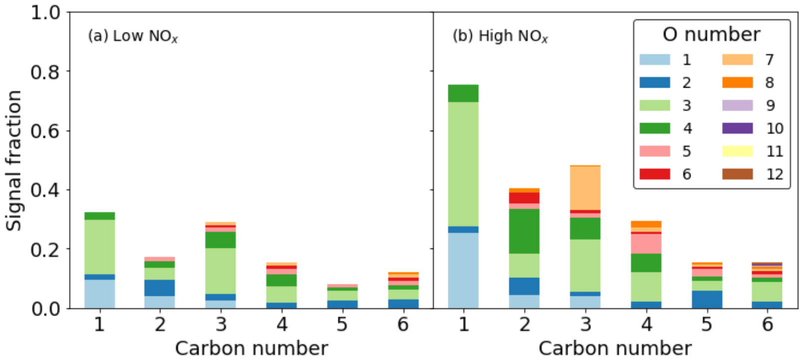

800 Figure 11. Signal fraction as a function of carbon number for ring breaking products for the (a) high NO$_x$ and (b) low NO$_x$ conditions.

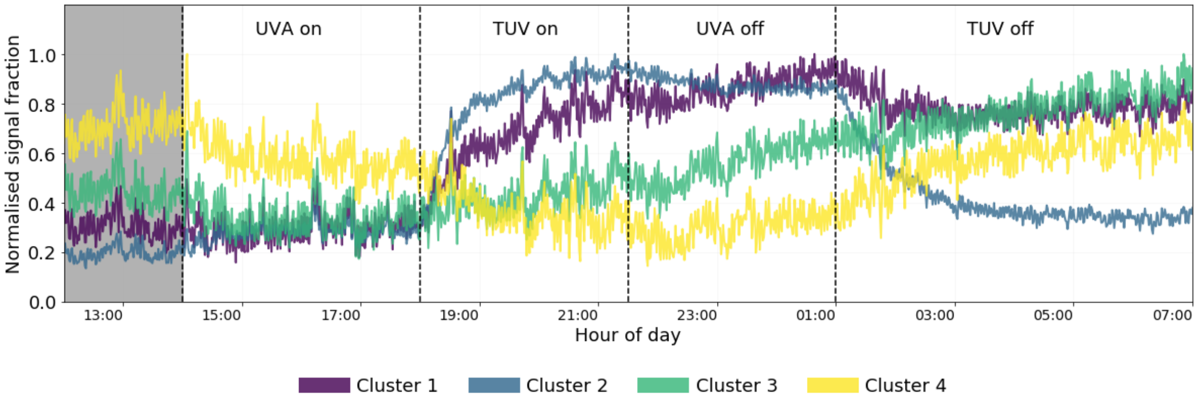

Figure 12. Time series of the four cluster means for the high NO_x experiment. Clusters 3 and 4 represent slow formation and background clusters and give no information regarding the effect of NO_2 photolysis. Clusters 1 and 2 display similar behaviours when the TUV light is switched on, but different behaviours when the UVA light is switched off, indicating their members are sensitive to the change NO/NO_x ratio determined by the UVA light state. The shaded area is the dark state before any photolysis occurs.

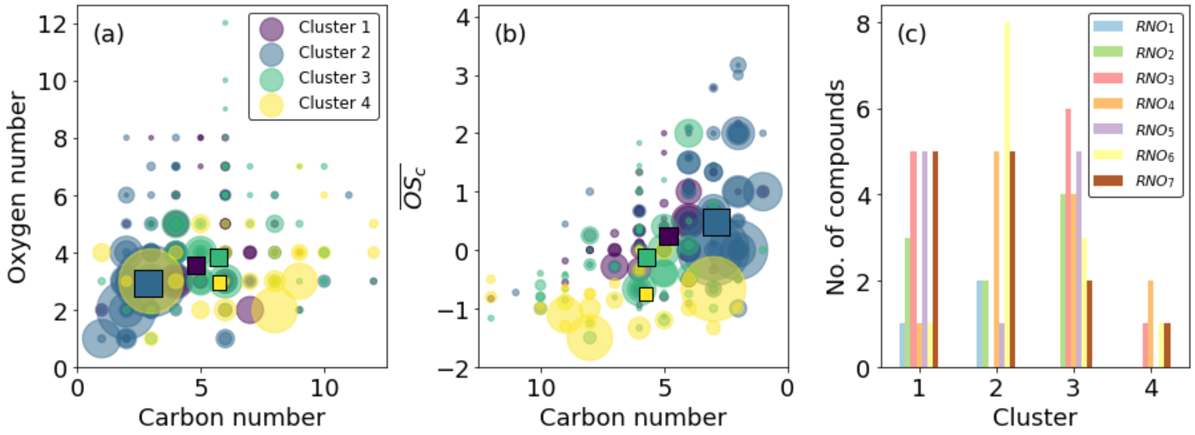

Figure 13. Cluster characteristics (a) carbon vs oxygen number (b) carbon number vs average carbon oxidation state. Squares indicate cluster averages. (c) Number of RNO_x species. Clustering based on time series similarity provides good separation in $\overline{OS_C}$ vs C space (b) and splits RNO_{odd} and RNO_{even} in clusters 1 and 2 (c).